Fusion Engineering and Design 189 (2023) 113477

Contents lists available at ScienceDirect

Fusion Engineering and Design

journal homepage: www.elsevier.com/locate/fusengdes

Advances in material phase change modelling approach for EU-DEMO limiter's plasma-facing components

M.L. Richiusa [a,b,*], P. Ireland [a], F. Maviglia [c], J. Nicholas [a], Z. Vizvary [b]

[a] Department of Engineering Science, Oxford Thermofluids Institute, University of Oxford, Oxford, OX2 0ES, UK
[b] UKAEA-CCFE, Culham Science Centre, Abingdon, Oxon, OX14 3DB, UK
[c] EUROfusion – Programme Management Unit, Boltzmannstrasse 2, Garching 85748, Germany

ARTICLE INFO

Keywords:
EU-DEMO limiters
Plasma-facing component
Melting
Vaporization
Arbitrary Lagrangian–Eulerian method

ABSTRACT

Within the EU-DEMO first wall protection framework, work on limiter's plasma-facing component design has started under plasma disruptive events (Richiusa et al., 2022). Starting from the rationale behind the TARTIFL&TTE software (Richiusa et al., 2022), this companion paper describes the progress on the engineering modelling of the plasma-facing material phase change under high heat flux, with the aid of COMSOL Multiphysics® software. The aim is to develop a reliable technique which can be used by designers for predicting how much of the solid armour undergoes phase change. This helps satisfy requirements for actively cooled components, such as at which armour depth safely locating the cooling system, and if its design can safely handle the heat transfer in the resulting component configuration after the disruption is extinguished. A few changes to the driving idea in Richiusa et al. (2022) will be also highlighted.

The multiphysics software allows us to implement a 1D model which can be extended to 2D/3D geometries subjected to both uniform and non-uniform heat flux. It also offers the capability of conjugated heat transfer in solids and liquids by coupling the two different domains. Although this multiphysics approach is also investigated, no effort in melting layer motion modelling is done. Therefore, the equivalent way of validating this approach while reducing its computational time is working with one single solid domain, within which any liquid phase changes are tracked by an *apparent heat capacity* formulation. The vapour domain is not modelled. The material removal due to the evaporative mass flux is modelled by means of moving mesh frames which push the recessing liquid interface backwards according to gas kinetics-driven boundary conditions. The melt pool is not removed during the transient. Mass balance considerations drive the liquid-to-vapour interface velocity.

The 3D Multiphisics implementation (3D-TARTIFL&TTE), is here supported by a benchmark activity and an application to the limiter's plasma-facing armour, whose preferred chosen thickness is 20 mm.

1. Introduction

Actively cooled sacrificial components, i.e. limiters, are foreseen within the EU-DEMO first wall protection strategy against off-normal plasma transients [1]. To fulfil the requirement of preserving the integrity of the cooling system following any damage to the limiter armour, the first step is estimating the thickness of material phase change absorbing the plasma energy release during disruptions. This drives the choice of locating the cooling system at a precise armour depth.

The investigation of this problem has already begun in [1]. The way the multi-phase moving boundary problem is approached, and implemented in MATLAB®, has brought to the creation of the TARTIFL&TTE (**T**hermal **A**nalysis fo**R** **T**racking **I**nter**F**aces under me**L**ting**&** vaporiza**T**ion-induced plasma **T**ransient **E**vents) software. The energy balance approach behind it has helped develop an understanding on the nature of this problem and the computational techniques to adopt. Although it needs improvements in the physics behind vaporization and the way it affects the energy balance, the computational implementation becomes more and more involving when going from 1D to more complex 3D geometries subjected to non-uniform heat flux. Since the methodology requires to be assessed, the aid of Multiphysics environment/software is sought as a step forward to equivalently reproduce the TARTIFL&TTE approach with both 2D/3D geometries and more complex physics. Therefore, the 3D-TARTIFL&TTE model implemented through COMSOL Multiphisics® is described hereafter, highlighting the main differences with TARTIFL&TTE.

* Corresponding author at: UKAEA-CCFE, Culham Science Centre, Abingdon, Oxon, OX14 3DB, UK.
E-mail address: lorena.richiusa@ukaea.uk (M.L. Richiusa).

https://doi.org/10.1016/j.fusengdes.2023.113477
Received 10 October 2022; Received in revised form 19 December 2022; Accepted 9 January 2023
Available online 30 January 2023

2. 3D-TARTIFL&TTE description

The TARTIFL&TTE stepwise approach of breaking down the heat transfer process in three phases, i.e. heat up, melting and vaporization, is replaced by a single transient thermal analysis. Any phase change is triggered and tackled within a single solid geometry domain.

In the 3D-TARTIFL&TTE, the solid-to-liquid phase change is tracked within the solid domain by means of the *apparent heat capacity* formulation [2]. It describes and solves the thermal problem by using one energy balance equation (Eq. (1)) that does not involve any latent heat. It assumes, instead, that the solid-to-liquid phase change occurs over the predefined temperature interval $T_m - \frac{\Delta T}{2}$ and $T_m + \frac{\Delta T}{2}$. The latent heat of fusion enters into the definition of *effective material properties* (see Eq. (2) for heat capacity, Eq. (4) for thermal conductivity and Eq. (5) for density definitions [2]), which are calculated from the temperature-dependent material property values assigned to every phase. The specific heat capacity is redefined as in Eq. (2), and encompasses the liquid and solid specific heat capacities plus the enthalpy ($\delta H = H_l - H_s = H_m$) required by the mass fraction α_m to change state. The transition is tracked by means of a temperature-dependent phase indicator Ω, whose value ranges between [0,1]. Before melting, $\Omega_s = 1$ and $\Omega_l = 1 - \Omega_s = 0$, whereas $\Omega_s = 0$ and $\Omega_l = 1$ if only liquid phase is present. The mass fraction α_m ranges from [−1/2,+1/2] for, respectively, solid and liquid phases [2]. The position of the melting interface over time is tracked by means of linear projections adopted for integrating Ω_l within the volume of the geometric domain.

$$\frac{\partial H}{\partial t} = \frac{\partial H}{\partial T}\frac{\partial T}{\partial t} = c^A \frac{\partial T}{\partial t} = \nabla \cdot (k^A \nabla(T)) \tag{1}$$

$$c^A = \frac{1}{\rho^A}(\Omega_s \rho_s c_{p,s} + \Omega_l \rho_l c_{p,l}) + \delta H \frac{\partial \alpha_m}{\partial T} \tag{2}$$

$$\alpha_m = \frac{1}{2}\frac{\Omega_l \rho_l - \Omega_s \rho_s}{\rho^A} \tag{3}$$

$$k^A = \Omega_s k_s + \Omega_l k_l \tag{4}$$

$$\rho^A = \Omega_s \rho_s + \Omega_l \rho_l \tag{5}$$

In line with the TARTIFL&TTE approach, the vapour domain is not simulated. While TARTIFL&TTE removes the vapour phase once formed by leaving the surface at the fixed boiling temperature T_v, 3D-TARTIFL&TTE simulates the vaporization phase by means of boundary conditions imposed on the top surface of the liquid layer. The vapour phase contribution to the energy balance is calculated through the estimate of the evaporative mass flux departing from the liquid layer after reaching the boiling point. Only at that point the contribution of the evaporative heat flux becomes consistently high to decrease the incoming heat flux magnitude, without the need of imposing a threshold boiling temperature value to trigger this phase change. Furthermore, in the 3D-TARTIFL&TTE the surface temperature is allowed to adjust its value in accordance with the saturation pressure, which affects the amount of the evaporative mass flux at every time instant. This affects, in turn, the surface temperature.

In summary, the heat flux absorbed by the domain (HF_{abs}) as sensible and latent heat of fusion results from a balance between the incoming space-and-time-varying heat flux (HF_{in}) and the outgoing energy contributions due to either evaporative (HF_v) and radiative (HF_{rad}) heat fluxes. As a result of this balance, the heat flux applied on the front face of the loaded component is computed as in Eq. (6). The evaporative heat and mass fluxes are evaluated by using the gas kinetics approach (Hertz–Knudsen–Langmuir law, Eq. (7)), where the retro-diffusion coefficient $\beta_R = 0.18$ [3] accounts for the fraction of evaporated particles which re-condensates after interacting with the surrounding gas. M and R are, respectively, the molar mass [g mol^{-1}] and the universal gas constant ($R = 8.314$ J mol^{-1} K^{-1}).

The radiative heat flux depends on the temperature-dependent surface emissivity (ε) and the Stefan–Boltzmann constant ($\sigma_b = 5.6704 \cdot 10^{-8}$ W m^{-2} K^{-4}).

$$HF_{abs} = HF_{in} - HF_v - HF_{rad} \tag{6}$$

where:

$$HF_v = (1 - \beta_R)\sqrt{\frac{M}{2\pi RT}} P_{sat}(T) H_v = \dot{m} H_v \tag{7}$$

$$HF_{rad} = \varepsilon \sigma_b \left(T_{front}^4 - T_{amb}^4\right). \tag{8}$$

Another difference between the two models is how the phase change is computationally tackled. The Stefan conditions applied at the interphase boundaries (see Eq. 12 and Eq. 22 in [1]) introduce a non-linearity within the TARTIFL&TTE formulation. Hence the use of the Landau transformation for fixing in space the energy balance-driven moving interfaces, and allowing the classical numerical techniques to be deployed. In the 3D-TARTIFL&TTE, the evaporative mass flux pushes the surface of the condensed domain back, which unavoidably deforms under mass loss. This recession is simulated by using the Lagrangian–Eulerian approach [2] (ALE, already implemented in COMSOL Multiphisics®) with a deformed mesh domain whose front face recessive velocity (v_v, Eq. (9)) is defined by imposing the mass continuity condition at the front face.

$$v_v = \frac{\dot{m}}{\rho_l} \tag{9}$$

For helping the software solve the computational problem, while avoiding the presence of distorted elements under a deforming domain, the velocity of the moving interface v_v is not imposed directly. It is instead used for calculating the equivalent deformation of every spatial point undergoing vaporization (see Eq. (10), with a damping factor d_a equal to 1 and a null mass coefficient $e_a = 0$). The spatial displacement is imposed as boundary condition through the definition of the Partial Differential Equation (Boundary PDE) in Eq. (10). The vapour-to-liquid interface is tracked by storing the average and maximum displacement values over time.

$$e_a \frac{\partial^2 x_v}{\partial t^2} + d_a \frac{\partial x_v}{\partial t} = v_v \tag{10}$$

A 2D sketch of the 3D domain subjected to phase change is shown in Fig. 1.

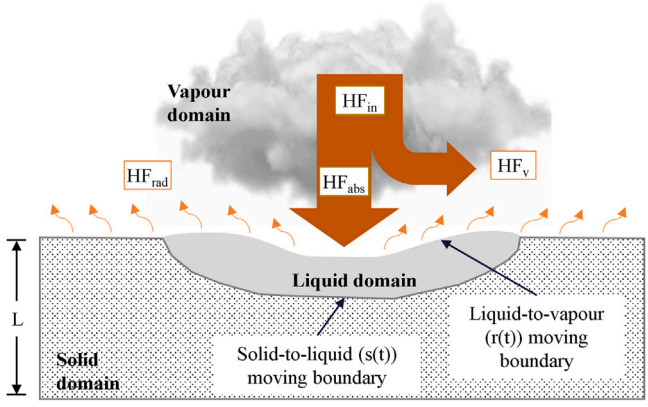

Fig. 1. 2D visual sketch of 3D-TARTIFL&TTE implementation. The outgoing heat flux HF_{out}, i.e. the sum of all the contributions decreasing the amount of energy absorbed by the domain as sensible and latent heat of fusion, includes HF_{rad}, HF_v and any potential vapour shielding effects that are not yet modelled.

3. Validation activity

The model needs to be validated for understanding its level of reliability under high heat flux. Since there are not data available in literature to be reproduced with high fidelity, either because of lack of clear input data, or because of the different goal of the performed experiments, dedicated experiments are going to be planned. To this purpose, high heat flux irradiation facilities are sought. The two main facilities identified for supporting the validation activity are: QSPA Kh-50 (Ukraine), and GLADIS (Germany). The preliminary validation of

the computational model is here based on data generated from past experiments run in QSPA (see Section 3.1). Unfortunately, due to the current international circumstances, QSPA is no longer available for running new dedicated experiments. The experimental campaign is instead planned to happen in the GLADIS facility, whose description and results will be highlighted in a future paper.

3.1. Benchmark against semi-experimental data from QSPA Kh-50

The Quasi-Stationary Plasma Accelerator (QSPA Kh-50) [4–6] is the largest worldwide plasma accelerator with unique plasma conditions. It is hosted by the Institute of Plasma Physics in Kharkov (Ukraine), and it can deliver an average heat flux of 4 GW m^{-2} over a 0.18 m-diameter footprint during a 0.25 ms pulse. It has been used for running experiments devoted to vapour shielding investigations, although very little is available in terms of experimental output data, due to the lack of high-sensitivity diagnostics characterizing this facility. Before the facility became unavailable in early 2022, a mix of both experimental and computationally reconstructed data have been collected and provided by Ukrainian researchers [7–10], which are here used for an assessment of the 3D-TARTIFL&TTE.

The provided data are related to shots where 5 × 5 × 1 cm^3 pure tungsten samples are loaded for 0.25 ms with a 6 GW m^{-2}-peaked triangularly time-varying heat flux profile over a 3 cm-diameter footprint, which is defined by a Mo diaphragm with an aperture of 3 cm installed in front of the W target to provide a clear-cut spot loaded with uniform power density [7]. Among the measured data, i.e. plasma density, pressure, velocity, and integrated energy density absorbed by the target, only the last one is used in the present work. All the other output parameters indicated hereafter as “reference”, such as the surface temperature evolution, heat flux and time evolution of the molten layer depth have been inversely reconstructed in [7,9] by means of the PEGASUS-3D software [8]. The data on molten layer depth and vaporized thickness come from post-mortem analyses on loaded samples [10].

Two shots are here taken as reference. Fig. 2 shows on the right-hand side (rhs) the sample and its footprint subjected to two triangularly-shaped heat flux evolutions, i.e. HF_1 and HF_2, respectively, plotted on the left-hand side (lhs). E_{abs_1} = 0.75 MJ m^{-2} and E_{abs_2} = 1.51 MJ m^{-2} are, respectively, the integrated absorbed energy densities for the two lhs heat flux profiles in Fig. 2. The rest of the provided data are listed in Table 1, where they are compared with the related data calculated by 3D-TARTIFL&TTE. Fig. 3 compares the time evolution of the surface temperatures, whereas the molten layer depths are reported in Fig. 4. Figs. 5 and 6 plot other output parameters calculated by 3D-TARTIFL&TTE, such as the vapour interface, its velocity, the evaporative heat flux and the absorbed energy density over time.

The input heat flux is applied at every time step along the fixed plasma stream direction, whose peak over time is increased by 0.5 MW m^{-2} to overcome the smoothing introduced by the boundary PDE used for imposing the deformation simulating the evaporative mass removal.

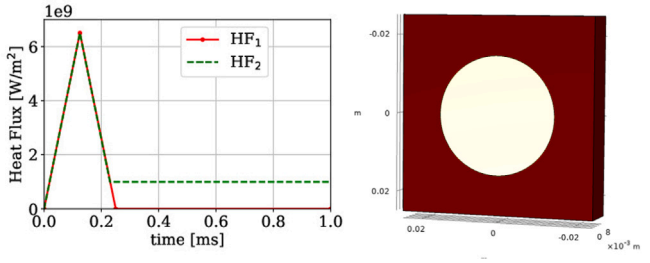

Fig. 2. Time-dependent heat flux values (lhs) applied over the 3 cm-diameter footprint of the rhs sample.

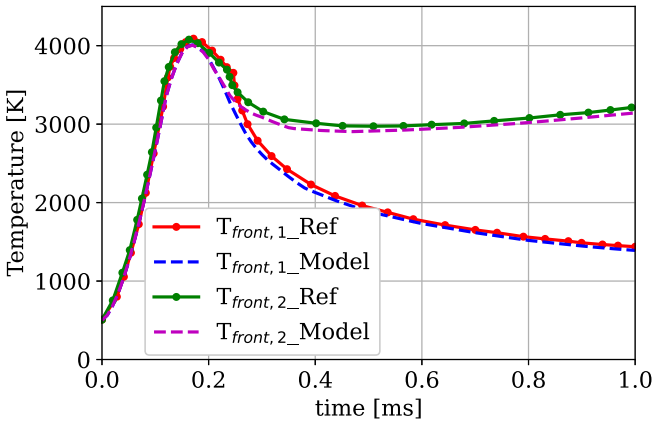

Fig. 3. Time evolution of the reference VS modelled surface temperatures under the applied HF_1 and HF_2 profiles.

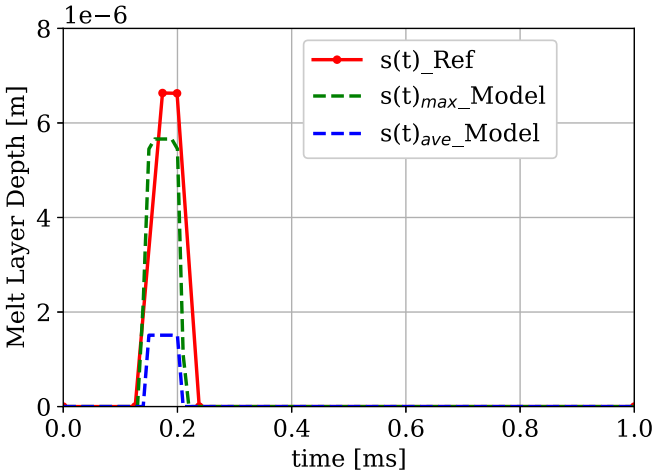

Fig. 4. Time evolution of the reference solid-to-liquid interface position VS the calculated one. Both the maximum and the average modelled values are here reported.

The reference value of the integrated absorbed energy density is 1.51 MJ m^{-2}. The calculated one is 1.57 MJ m^{-2}, considering the increase of the maximum value of the input heat flux by 8%.

In terms of molten and vaporized layer depths, indicated respectively as s(t) and r(t), the two heat flux profiles produce the same effect. 3D-TARTIFL&TTE starts experiencing melting ($T_{front} = T_m$ = 3695 K [11]) at 0.14 ms, while solidification at 0.21 ms. The reference data highlight that the melting layer starts appearing at 0.1 ms, and it solidifies at 0.23 ms. The maximum modelled molten layer depth is 5.7 μm against the reference 6.6 μm. This leads to a preliminary satisfactory conclusion on the 3D-TARTIFL&TTE approach, being able to match the key-output parameters, i.e. surface temperature and melt layer depth, with a 3D domain undergoing non-uniform heat flux.

As for the surface recession due to vaporization, the calculated maximum value of the surface deformation is 0.018 nm, meaning that vaporization is negligible ($T_{front} \ll T_v \approx$ 5900 K [12]) and only a moderate evaporative mass flux leaves the surface. The authors in [10] estimated the average erosion rate to be ≈30 nm/pulse for tungsten samples subjected to repetitive QSPA pulses with 1.1 MJ m^{-2} energy density, being this value 10 times less for pulses delivering 0.7 MJ m^{-2}. However, they underline that for initial pulses the boiling is initiated on the surface by impurities, and only after 25 pulses it becomes a volumetric phenomenon which contribute to mass losses possibly due to intensification of evaporation and tungsten splashing. Although 3D-TARTIFL&TTE can deal with vaporization, impurities effects, splashing

Table 1
QSPA Kh-50 data for validation provided by Ukrainian researchers [7–10].

	Reference	Calculated	Error
HF_{max1}/HF_{max2} [GW m^{-2}]	6.0/6.0	6.5/ 6.5	8%
E_{abs1}/E_{abs2} [MJ m^{-2}]	0.75/1.51	0.81/1.57	8%/4%
t_m [ms]	0.13	0.14	8%
t_{solid} [ms]	0.23	0.21	9%
$T_{front,max}$ [K]	4089	4011	2%
Melt layer [μm/pulse]	6.6	5.7	14%

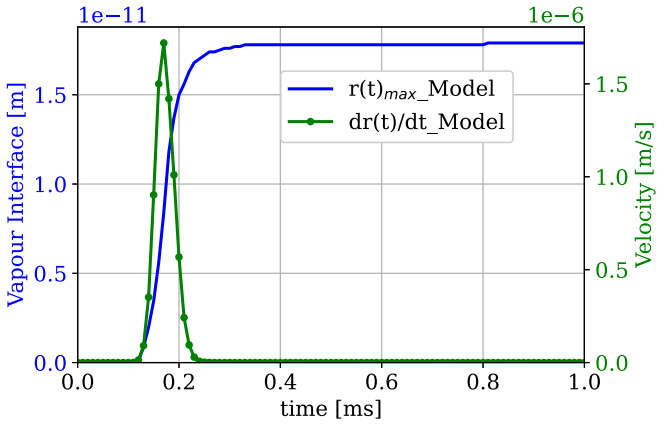

Fig. 5. Modelled liquid-to-vapour interface position over time and surface recession velocity due to vaporization.

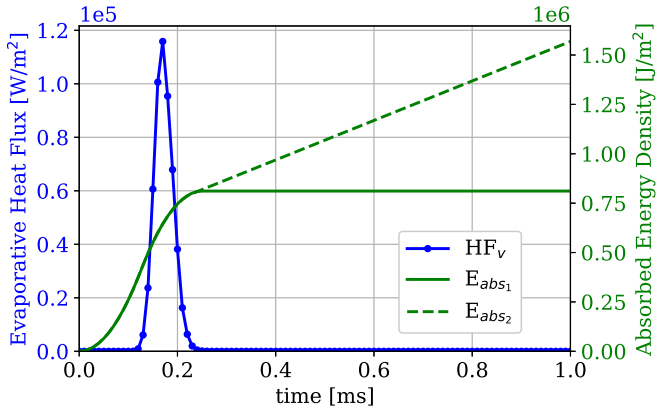

Fig. 6. Time evolution of the calculated HF_v and deposited energy density E_{abs}.

and melt motion are not captured. Therefore, no unambiguous conclusion based on common assumptions can be here stated on the modelled vapour layer.

4. EU-DEMO limiter PFC design

3D-TARTIFL&TTE has been used for studying the behaviour of EU-DEMO divertor tungsten monoblocks [13] as potential solutions for the sacrificial Upper Limiter (UL, Fig. 7) plasma-facing surface, with different armour thickness L – highlighted in Fig. 8 – under a heat load history typical of an Upward Vertical Displacement Events (UVDE) [14]. Starting from the thermal equilibrium reached during normal operation (Start-of-Flat Top, SOF, see Table 2), the monoblock experiences a sudden increase in heat flux following a VDE. Hence, during the plasma thermal quench (TQ), the heat flux goes up to 64 GW m^{-2} for 4 ms, for decreasing to 2.5 MW m^{-2} during the current quench (CQ) in the following 200 ms, in line with what has been foreseen for an UVDE in [14].

Table 2 lists the complete set of values of loads and boundary conditions used for the present work. Considerations based on energy

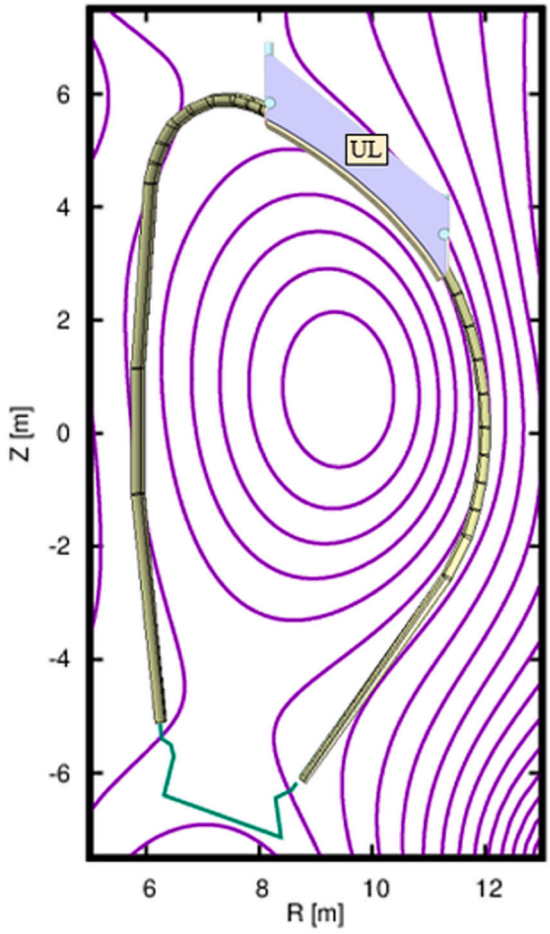

Fig. 7. Poloidal location of the Upper Limiter (UL) and plasma magnetic configuration during the UVDE TQ phase.

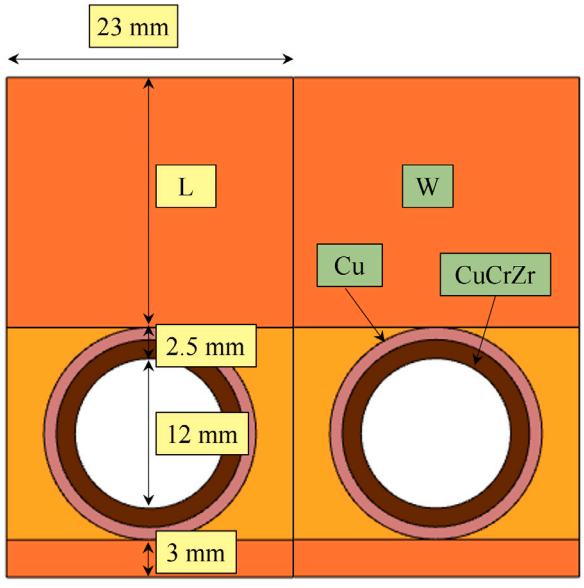

Fig. 8. 3D monoblock model used in the present work.

conservation principle have allowed the estimate of the bulk temperature of the coolant (water) and its heat transfer coefficients for the convective boundary conditions applied at the inner surface of the

pipes. The radiative power has been estimated by considering that the limiter is in view of the breeding blanket segments, whose surface temperature should not exceed 500 °C [15]. Therefore, the limiter radiates towards an ambient at 500 °C. Nuclear heating computed in [16] is also imposed as volumetric power generation across the tungsten monoblock.

As far as the material properties are concerned, temperature-dependent values for density, heat capacity, thermal conductivity, and emissivity taken from [17] have been imposed.

Four values of armour thickness have been spanned: 8 mm, 10 mm, 15 mm, and 20 mm. The results are reported in Table 3 in terms of maximum surface temperature, melting depth and total recession of the loaded surface, together with temperature and heat flux values computed at the inner surface of the pipe. Fig. 9 shows the time evolution of the temperature at the plasma-facing surface, and the related melt interface position during the transient, whereas Fig. 10 reports the time evolution of the temperature monitored at the inner pipe wall before and after the UVDE. Although the CQ is meant to last 200 ms, the runs have been stopped only after the thermal equilibrium is reached under CQ-induced heat flux.

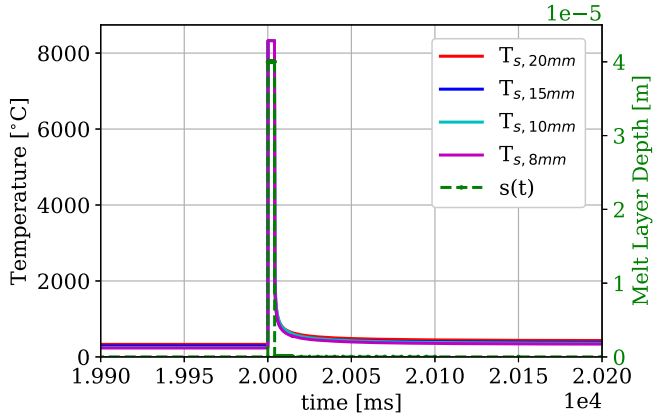

Fig. 9. Time evolution of the surface temperature and the melt interface under the heat load history foreseen during Upward VDEs.

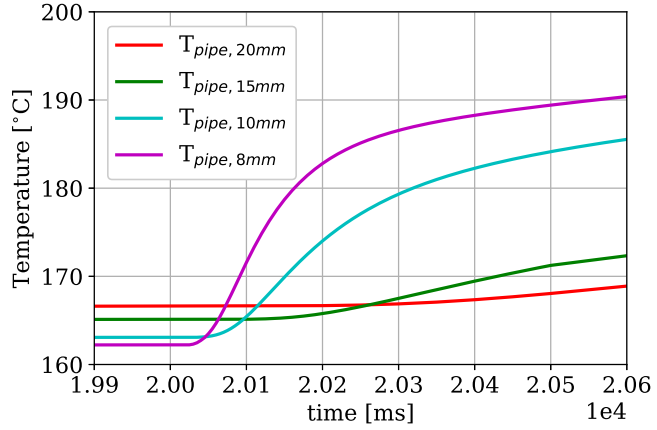

Fig. 10. Time evolution of the inner pipe wall temperature under the heat load history foreseen during Upward VDEs.

The parameters at the inner surface of the pipe are the ones to be monitored for understanding if the temperature increase experienced by the pipe is high enough to enhance onset of nucleate boiling/departure from nucleate boiling. The temperature limit is driven by the saturation temperature at the lowest value of the operational coolant pressure, which can be predicted through the Bergles-Rohsenow correlation [18], but it is in this case close to T_{sat}(5 MPa) = 264 °C. The heat flux should be limited to its critical heat flux value calculated at the inner wall of the pipe (CHF_w), which has been estimated by using the Tong-75 correlation [19] in Eq. (11).

$$CHF_w = 0.23 f G H_v \left(1 + 0.00216\left(\frac{P}{P_c}\right)^{1.8} Re^{0.5} Ja\right) C_f \tag{11}$$

Eq. (11) has been used for the water-cooled ITER divertor design, and directly correlates the CHF at the wall of smooth pipes to the mass flow rate G, Reynolds number, coolant pressure compared to its critical value (P_{crit} = 22.1 MPa), latent heat of vaporization (H_v), and Jakob number (Eq. (12)), through a friction factor f (Eq. (13)) depending on the ratio between the hydraulic diameter (d_h) and a reference diameter ($d_0 = 12.7 \cdot 10^{-3}$ m [19]), and the C_f factor accounting for channel configuration and dimension. For smooth channels, $C_f \approx 1.2$.

$$Ja = \frac{\rho_l}{\rho_v}\left(\frac{c_p(T_{sat} - T)}{H_V}\right) \tag{12}$$

$$f = 8Re^{-0.6}\left(\frac{d_h}{d_0}\right)^{0.32} \tag{13}$$

By using a first estimate of the coolant outlet pressure value (P = 4.3 MPa) and an average coolant bulk temperature (T_{ave} = 138 °C) for computing the Ja number, the resulting critical heat flux at the inner surface of the smooth pipes has found to be $CHF_w \approx 27$ MW m^{-2}.

5. Results

The benchmark reported in Section 3.1 shows good agreement between the reference and modelled data, especially in terms of maximum surface temperature and melting interface depth. Although the molten layer always stays in place during the loading condition, all the parameters agree well within 15% error. As for the vapour layer depth, no clear comparison can be established between the reference and the modelled data, due to the different conditions under which vaporization occurs both in experiments and computational modelling. This has to be added to the difficulty to reach experimental vaporization conditions well captured by diagnostics. If we assume the evaporative erosion rate as reference value, one explanation to this discrepancy might be related to the combined effects of heat flux acting on deforming mesh elements and the smoothing effect produced by the way the surface deformation is imposed through PDEs. This would explain why only the liquid-to-vapour interface tracking is affected, whereas the energy contribution is rightly captured as shown in Fig. 4. Three main points should be here argued: (a) the front face of the sample never reaches the boiling point (Fig. 3); (b) material impurity effects are not taken into account for the estimate of pure tungsten melting and boiling points; (c) average erosion rate in [4] is based on vaporization strongly affected by impurities during the first shots of a series of repetitive pulses. Therefore, due to lack of solid basis on which establishing any comparison on the vapour layer, the authors believe no final conclusions can be drafted yet, leaving the investigation of this aspect only after assessing the 3D-TARTIFL&TTE capability of correctly capturing the melt layer depth.

As far as the 3D-TARTIFL&TTE application to a 3D tungsten monoblock is concerned, the results in Table 3 show that during the transient event only the refractory armour withstands the plasma impact by means of its thermal inertia. During normal operation, the tungsten monoblock experiences a surface temperature below 350 °C, which increases up to ≈8300 °C during the TQ phase, no matter how thick the armour is, provided that there is enough material to withstand the heat wave. The sudden rise of the TQ thermal load leads the armour to instantaneously melt and intensively vaporize. Due to the short duration of the TQ, the intense vaporization prevents the molten layer to expand further against the solid domain, by reaching immediately its “steady-state” value. The phase change lasts for the entire duration of the TQ, after which the melt layer solidifies under the deformed configuration left by the vapour removal. The boiling temperature at the front face of the monoblock is not constrained to any value, since

Table 2
Summary of the heat loads and boundary conditions used for the monoblock thermal transient analyses.

	Loads and boundary conditions during Vertical Displacement Events (VDEs)		
	Start-of- Flat Top (SOF)	Thermal Quench (TQ)	Current Quench (CQ)
Δt [ms]	$2 \cdot 10^4$ [ms][a]	Δt = 4 [ms]	Δt = 200 [ms]
$HF_{SOF,TQ,CQ}$ [MW m^{-2}]	0.8	$6.4 \cdot 10^4$	2.52
$T_{bulk,water}$ [°C]/P [MPa]		138/5	
HTC [W m^{-2} K^{-1}]		$\sim 6 \cdot 10^4$	
$T_{irr,ext}$ [°C]		500	
Volumetric power generation [MW m^{-3}]		Tab. data: 20 (max) – 8 (min) [16]	

[a]Time to reach the thermal equilibrium.

Table 3
Armour thickness parametric thermal transient analysis results.

		Armour thickness (L) - preliminary results			
		8 [mm]	10 [mm]	15 [mm]	20 [mm]
Monoblock surface	$T_{max,SOF}/T_{max,TQ}/T_{max,CQ}$ [°C]	235/~8300/328	250/~8300/351	289/~8300/390	331/~8300/432
	Melt layer [mm]		~0.04		
	Surface deformation [mm]		~2.5		
Inner pipe surface	$T_{max,SOF}/T_{max,TQ}/T_{max,CQ}$ [°C]	~162/162/181	~163/163/173	~165/165/167	~167/167/167
	$HF_{max,CQ}$ [MW m^{-2}]	~2.5	~2	~1.6	~1.6

it depends on the saturation pressure and on the evaporative heat flux leaving the surface, as explained in Section 2. The same sharp and sudden temperature increase is experienced by the armour at the beginning and at the end of the TQ phase, and only under the CQ thermal loading the temperature of the inner surface of the pipe starts increasing, respectively, ≈300 ms and ≈50 ms after the TQ extinguishes with a 15 mm-and-20 mm-thick and 8 mm-and-10 mm-thick armours.

The coolant is not simulated as a domain but it is instead replaced by a convective condition imposed at the inner surface of the pipe walls, whose temperature is not affected by such a disruptive event until the disruption is actually extinguished. However, data in Table 3 shows that the thinner the armour thickness, the higher the temperature at the inner surface of the pipe, where both maximum temperature and incoming heat flux have been monitored. Although both temperature and heat flux at the inner wall of the pipe are well below their critical values, applications with the worst values of outlet coolant pressure and temperature have to verify that this condition will never be reached for the whole duration of the transient event. Therefore, among the investigated thicknesses, so far the first conservative choice of the armour "space reservation" is 20 mm for facing such transients. The equivalent configuration needs to be assessed thermo-mechanically during normal operation as well, for verifying that the monoblock layout does not suffer from high thermal stresses at the interface with the pipes.

6. Conclusions

Within the EU-DEMO first wall protection strategy, the engineering design workflow of any sacrificial components (i.e. limiters) withstanding off-normal plasma impacts requires any armour phase change to be considered, since it affects the cooling system design and integrity.

Efforts towards heat transfer modelling in presence of phase change has brought to the 3D-TARTIFL&TTE implementation. Its rationale, implemented as a 3D COMSOL Multiphysics® model, has shown so far good capability in predicting the energy contributions taking part in the phase change process. Starting from a solid domain undergoing high heat flux, the melting phase is triggered by an arbitrary temperature interval through the *apparent heat capacity* formulation, until it reaches the boiling temperature. At this point, the increasing evaporative mass flux, which is computed by using the Langmuir–Hertz–Knudsen law, absorbs a fraction of the incoming heat flux due to evaporation, by leaving a recessed surface behind it. The surface deformation is dictated by the recessive velocity, calculated by means of the mass continuity imposed at the vapour-to-liquid interface. The vapour domain is not physically modelled, but any effects related to the reduction of the incoming heat flux (i.e. due to vapour shielding) can be easily implemented as additional boundary conditions.

The first benchmark against QSPA data shows a good agreement on molten layer depth estimate, paving the way for its use within the engineering design workflow of metallic plasma-facing components.

The application of 3D-TARTIFL&TTE to a tungsten monoblock armour leads to a preferred chosen thickness of 20 mm, as a conservative preliminary value to be checked under pressure and temperature values calculated at the cooling system outlet.

A stepwise validation activity is foreseen in the near-term future, to further support the benchmark of the 3D-TARTIFL&TTE approach and drive its way of modelling the phase changes, especially when they involve intense vaporization. Therefore, as a step forward, a dedicated campaign of melting experiments is foreseen in the GLADIS facility to support a further validation of the model. The results of this experimental validation will be published in a future paper.

CRediT authorship contribution statement

M.L. Richiusa: Conceptualization, Methodology, Formal analysis, Software, Validation, Investigation, Visualization, Writing – review & editing. **P. Ireland:** Supervision, Project administration, Review & editing. **F. Maviglia:** Supervision, Project administration. **J. Nicholas:** Supervision. **Z. Vizvary:** Supervision, Review & editing.

Declaration of competing interest

The authors declare that they have no known competing financial interests or personal relationships that could have appeared to influence the work reported in this paper.

Data availability

Data will be made available on request.

Acknowledgements

This work has been carried out within the framework of the EUROfusion Consortium, funded by the European Union via the Euratom Research and Training Programme (Grant Agreement No 101052200 — EUROfusion). Views and opinions expressed are however those of the author(s) only and do not necessarily reflect those of the European Union or the European Commission. Neither the European Union nor

the European Commission can be held responsible for them. The authors would like to thank the Ukraininan researchers Igor Garkusha, Vadym Makhlaj, and Stanislav Herashchenko for providing some useful data from QSPA Kh-50 in support of this work, as well as their expressed support towards future experimental collaborations.

References

[1] M.L. Richiusa, P. Ireland, J. Nicholas, Z. Vizvary, Rationale behind eu-demo limiter's plasma-facing component design under material phase change, IEEE Trans. Plasma Sci. (2022) 1–7.

[2] COMSOL Multiphysics®. COMSOL Multiphysics Reference Manual. https://doc.comsol.com/5.5/doc/com.comsol.help.comsol/COMSOL_ReferenceManual.pdf.

[3] S.I. Anisimov, Vaporization of Metal Absorbing Laser Radiation, Vol. 27, World Scientific, 1996, pp. 14–15.

[4] V.I. Tereshin, Quasi-stationary plasma accelerators (QSPA) and their applications, Plasma Phys. Control. Fusion 37 (11A) (1995).

[5] A.I. Morozov, O.A. Shchurov, O.S. Pavlichenko, V.I. Tereshin, V.V. Chebotarev, Ya.F. Volkov, V.I. Kovalenko, Kulik, V. N., V.S. Manojlo, V.V. Marinin, D.G. Solyakov, V.V. Stal'tsov, Yu.I. Tashchev, B.Yu. Tsupko, Qspa kh-50 full-scale high-power asistationary plasma accelerator, Plasma Devices Oper. 2 (2) (1992) 155–165.

[6] V.I. Tereshin, I.E. Garkusha, A.N. Bandura, O.V. Byrka, V.V. Chebotarev, V.A. Makhlaj, D.G. Solyakov, H. Wuerz, Influence of plasma pressure gradient on melt layer macroscopic erosion of metal targets in disruption simulation experiments, J. Nucl. Mater. 313-316 (SUPPL.) (2003) 685–689.

[7] I.E. Garkusha, A.N. Bandura, O.V. Byrka, V.V. Chebotarev, I. Landman, V.A. Makhlaj, S. Pestchanyi, V.I. Tereshin, Damage to preheated tungsten targets after multiple plasma impacts simulating ITER ELMs, J. Nucl. Mater. 386–388 (C) (2009) 127–131.

[8] S. Pestchanyi, H. Würz, Brittle destruction of carbon based materials under off-normal ITER-FEAT conditions, Phys. Scripta T 91 (2001) 84–89.

[9] S. Pestchanyi, I. Garkusha, V. Makhlaj, I. Landman, Estimation of the dust production rate from the tungsten armour after repetitive elm-like heat loads, Phys. Scripta, T 145 (2011) 014062.

[10] V.I. Tereshin, A.N. Bandura, O.V. Byrka, V.V. Chebotarev, I.E. Garkusha, I. Landman, V.A. Makhlaj, D.G. Solyakov, A.V. Tsarenko, Repetitive plasma loads typical for ITER type-I ELMS: Simulation in QSPA Kh-50, AIP Conf. Proc. 812 (2006) (2006) 128–135.

[11] P. Tolias, Analytical expressions for thermophysical properties of solid and liquid tungsten relevant for fusion applications, Nucl. Mater. Energy 13 (2017) 42–57.

[12] NIST Chemistry WebBook. Tungsten. https://webbook.nist.gov/cgi/inchi/InChI%3D1S/W.

[13] J.H. You, G. Mazzone, E. Visca, H. Greuner, M. Fursdon, Y. Addab, C. Bachmann, T. Barrett, U. Bonavolontà, B. Böswirth, F.M. Castrovinci, C. Carelli, D. Coccorese, R. Coppola, F. Crescenzi, G. Di Gironimo, P.A. Di Maio, G. Di Mambro, F. Domptail, D. Dongiovanni, G. Dose, D. Flammini, L. Forest, P. Frosi, F. Gallay, B.E. Ghidersa, C. Harrington, K. Hunger, V. Imbriani, M. Li, A. Lukenskas, A. Maffucci, N. Mantel, D. Marzullo, T. Minniti, A.V. Müller, S. Noce, M.T. Porfiri, A. Quartararo, M. Richou, S. Roccella, D. Terentyev, A. Tincani, E. Vallone, S. Ventre, R. Villari, F. Villone, C. Vorpahl, K. Zhang, Divertor of the european demo: Engineering and technologies for power exhaust, Fusion Eng. Des. 175 (2022) 113010.

[14] F. Maviglia, C. Bachmann, G. Federici, T. Franke, M. Siccinio, R. Albanese, R. Ambrosino, W. Arter, R. Bonifetto, G. Calabrò, R. De Luca, L.E. Di Grazia, E. Fable, P. Fanelli, A. Fanni, M. Firdaouss, J. Gerardin, R. Lombroni, M. Mattei, M. Moscheni, W. Morris, G. Pautasso, S. Pestchanyi, G. Ramogida, M.L. Richiusa, G. Sias, F. Subba, F. Villone, J. You, Z. Vizvary, Integrated design strategy for eu-demo first wall protection from plasma transients fusion engineering and design 177 (2022) 113067, Fusion Eng. Des. 178 (2022) 113125.

[15] D. Stork, P. Agostini, J.L. Boutard, D. Buckthorpe, E. Diegele, S.L. Dudarev, C. English, G. Federici, M.R. Gilbert, S. Gonzalez, A. Ibarra, Ch. Linsmeier, A. Li Puma, G. Marbach, P.F. Morris, L.W. Packer, B. Raj, M. Rieth, M.Q. Tran, D.J. Ward, S.J. Zinkle, Developing structural, high-heat flux and plasma facing materials for a near-term DEMO fusion power plant: The EU assessment, J. Nucl. Mater. 455 (1–3) (2014) 277–291.

[16] A. Cufar, Radial Profile of Nuclear Heating in Upper Port Limiter, Technical report, EUROfusion IDM, 2022, https://idm.euro-fusion.org/?uid=2P9L5K&action=get_document.

[17] ITER Organization, Iter Material Property HandBook, Technical report, ITER Organization, 2017, https://user.iter.org/Portal/Pages/ContentView.aspx?uid=2239QQ.

[18] N.E. Todreas, M.S. Kazimi, Nuclear Systems Volume I: Thermal Hydraulic Fundamentals, third ed., CRC Press, 2021.

[19] A.R. Raffray, J. Schlosser, M. Akiba, M. Araki, S. Chiocchio, D. Driemeyer, F. Escourbiac, S. Grigoriev, M. Merola, R. Tivey, G. Vieider, D. Youchison, Critical heat flux analysis and r & d for the design of the iter divertor, Fusion Eng. Des. 45 (4) (1999) 377–407.